Rubio, M., Montanero, J. M., Eggers, J. G., & Herrada, M. A. (2023). Stable production of fluid jets with vanishing diameters via tip streaming. Manuscript submitted for publication.

Early version, also known as pre-print

University of Bristol - Explore Bristol Research
General rights

1

Stable production of fluid jets with vanishing diameters via tip streaming

M. Rubio[1], J. M. Montanero[2], J. Eggers[3], M. A. Herrada[4]

[1]Depto. de Ingeniería Energética y Fluidomecánica and
Instituto de las Tecnologías Avanzadas de la Producción (ITAP), Universidad de Valladolid,
E-47003 Valladolid, Spain

[2]Departamento de Ingeniería Mecánica, Energética y de los Materiales and
Instituto de Computación Científica Avanzada (ICCAEx),
Universidad de Extremadura, E-06071 Badajoz, Spain

[3]School of Mathematics, University of Bristol, Fry Building, Bristol BS8 1UG, UK

[4]Departamento de Ingeniería Aeroespacial y Mecánica de Fluidos,
Universidad de Sevilla, E-41092 Sevilla, Spain

We study numerically the microjetting mode obtained when a fluid is injected through a tube submerged in a uniaxial extensional flow. The steady solution to the full non-linear Navier-Stokes equations is calculated. We obtain the linear global modes determining the linear stability of the steady solution. For sufficiently large outer viscosity, the flow remains stable for infinitely small values of the injected flow rate. This implies that jets with vanishing diameters can be produced regardless of the jet viscosity and outer flow strength. For a sufficiently small inner-to-outer viscosity ratio, the microjetting instability is associated only with the flow near the entrance of the jet. The tapering meniscus stretches and adopts a slender quasi-conical shape. Consequently, the cone tip is exposed to an intense outer flow, which stabilizes the flow in the cone-jet transition region. This work presents the first evidence that fluid jets with arbitrarily small diameters can be stably produced via tip streaming.

1. Introduction

The stable production of arbitrarily thin fluid jets has become the Holy Grail for many microfluidic applications that demand monodisperse collections of tiny droplets, bubbles, capsules, and emulsions. The microjetting mode of tip streaming (Anna & Mayer 2006; Montanero & Gañán-Calvo 2020) has been the preferred method in most cases because it allows the formation of long fluid threads much thinner than any fluid passage of the microfluidic device. Using hydrodynamic (De Bruijn 1993) or electrohydrodynamic forces (Duft *et al.* 2003), energy is gently focused into the tip of a tapering meniscus anchored to the feeding tube. In a particular region of the parameter space, the meniscus tip steadily emits a jet much thinner than the tube. The jet eventually breaks up into droplets due to the capillary instability.

The kinetic energy per unit volume $\rho_j v_j^2/2$ (ρ_j and v_j are the jet's density and velocity, respectively) is practically independent of the injected flow rate Q in most microjetting realizations. This implies that the jet diameter $d_j \sim (Q_i/v_j)^{1/2}$ scales approximately as $Q_i^{1/2}$. In principle, the jet diameter can be indefinitely reduced by lowering the injected flow rate. However, experiments and numerical simulations have shown that the

flow inevitably becomes unstable at a critical value of Q_i, which sets a minimum value of the jet diameter (Montanero & Gañán-Calvo 2020). For instance, the microjetting modes of gravitational jets (Rubio-Rubio *et al.* 2013), flow focusing (Cruz-Mazo *et al.* 2017), confined selective withdrawal (Evangelio *et al.* 2016; López *et al.* 2022), and electrospray (Ponce-Torres *et al.* 2018) become unstable at this well-known minimum flow rate stability limit, which prevents producing jets with arbitrarily small diameters.

A number of significant studies of the microjetting mode of tip streaming demonstrated thin jets, but that did not determine the minimum flow rate stability limit. Using a double flow-focusing arrangement, Gañán-Calvo *et al.* (2007) produced compound fluid jets with submicrometer diameters. The transient numerical simulations of Suryo & Basaran (2006) showed the transition from jetting to microjetting (tip streaming) in the coflowing configuration when the inner-to-outer flow rate ratio decreased below a critical value. The vanishing flow rate ratio limit was not analyzed in that work. It is worth mentioning that Gañán-Calvo (2008) showed that an infinitely thin jet is stable (convectively unstable) if the interface speed exceeds a critical value, which depends on the ratio between the jet and outer medium viscosities. However, this must be regarded as a prerequisite for microjetting, which does not consider the critical instability that originates in the tapering meniscus.

Taylor (1932, 1934) proposed a long-wave model to describe the flow in an axisymmetric drop submerged in a viscous uniaxial extensional flow. Using this approximation, Zhang (2004) showed how the extensional flow might produce a vanishingly thin jet from the tip of a meniscus attached to a tube. A continuous transition to microjetting with an arbitrarily small flow rate (jet diameter) can occur when the imposed capillary number is decreased. As the flow rate decreases, the solution to the long-wave model tends to a universal velocity profile when the variables are appropriately scaled. However, these numerical results were based on the slender body theory, which is known to fail for conical tips (Eggers 2021). More importantly, the flow stability was not determined, and, therefore, the viability of this method was not demonstrated. It must be pointed out that numerical simulations usually converge to a microjetting solution even when the bifurcation point has been crossed, making the stability analysis critical.

This work examines the microjetting mode obtained when a fluid is injected through a tube submerged in a uniaxial extensional flow $(-Gr/z, 0, Gz)$. We analyze the flow stability as the injected flow rate decreases. Our results show that infinitely thin jets can be produced for a sufficiently large outer viscosity, independently of the jet viscosity and the outer flow intensity G.

2. Governing equations

Consider a cylindrical capillary of radius a placed in linear uniaxial extensional flow given by the equations

$$u^{(o)} = -Gr/2, \quad w^{(o)} = G z, \tag{2.1}$$

where $u^{(o)}$ and $w^{(o)}$ are the radial and axial components of the velocity field, and G is the flow intensity. The center of the capillary exit is located at the origin of the cylindrical coordinate system (r,z) (see Fig. 1). A fluid of density ρ_i and viscosity μ_i is injected through the capillary at a constant flow rate Q_i. The density and viscosity of the outer fluid are ρ_o and μ_o, respectively, and the surface tension of the interface is σ.

Hereafter, all the variables are made dimensionless with the characteristic length a, velocity σ/μ_0, time $\mu_o a/\sigma$, and stress σ/a. The dimensionless, axisymmetric, incompress-
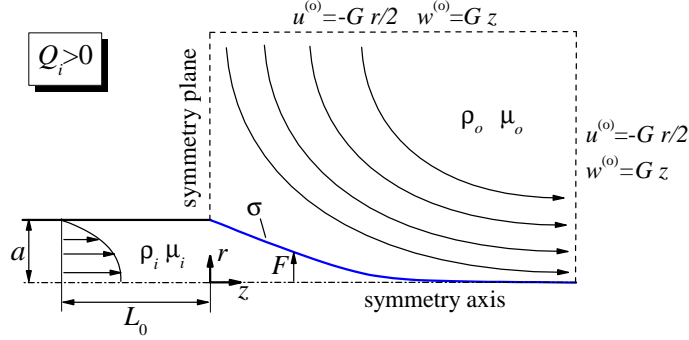
FIGURE 1. Sketch of the fluid domain for $Q > 0$. The dashed line indicates the computational domain.

ible Navier-Stokes equations for the velocity and pressure fields are

$$[ru^{(k)}]_r + rw_z^{(k)} = 0, \tag{2.2}$$

$$(\lambda^2)^{\delta_{ik}}\mathrm{Re}_k[u_t^{(k)} + u^{(k)}u_r^{(k)} + w^{(k)}u_z^{(k)}] = -p_r^{(k)} + \lambda^{\delta_{ik}}[u_{rr}^{(k)} + (u^{(k)}/r)_r + u_{zz}^{(k)}], \tag{2.3}$$

$$(\lambda^2)^{\delta_{ik}}\mathrm{Re}_k[w_t^{(k)} + u^{(k)}w_r^{(k)} + w^{(k)}w_z^{(k)}] = -p_z^{(k)} + \lambda^{\delta_{ik}}[w_{rr}^{(k)} + w_r^{(k)}/r + w_{zz}^{(k)}], \tag{2.4}$$

where $u^{(k)}$ ($w^{(k)}$) is the radial (axial) velocity component, $p^{(k)}$ is the pressure field, $\mathrm{Re}_k = \rho_k \sigma a/\mu_k^2$ is the Reynolds number (the inverse of the Ohnesorge number) of phase k, $\lambda = \mu_i/\mu_o$ is the viscosity ratio, and δ_{ij} is the Kronecker delta. In the above equations and henceforth, the subscripts and superscripts $k = i$ and o refer to the inner and outer phases, respectively, and the subscripts t, r, and z denote the partial derivatives with respect to the corresponding variables. The action of the gravitational field has been neglected due to the smallness of the fluid configuration.

The kinematic compatibility condition at the interface reads

$$F_t + F_z w^{(i)} - u^{(i)} = F_t + F_z w^{(o)} - u^{(o)} = 0, \tag{2.5}$$

where $F(z,t)$ is the distance of an interface element to the symmetry axis z. We consider the continuity of the velocity field $\mathbf{v}^{(k)}(r, z; t)$ and tangential stress at the interface, as well as the normal stress jump due to the capillary pressure:

$$||\mathbf{v}^{(k)}|| = \mathbf{0}, \quad ||\tau_t^{(k)}|| = 0, \quad ||\tau_n^{(k)}|| = \kappa, \tag{2.6}$$

where $||A^{(k)}||$ denotes the difference $A^{(i)} - A^{(o)}$ between the values taken by the quantity A on the two sides of the interface, $\tau_t^{(k)}$ and $\tau_n^{(k)}$ and represent the tangential and normal stress, respectively, and κ is the local mean curvature.

The triple contact line anchorage condition, $F = 1$, is set at the capillary edge. We impose the velocity field $u^{(o)} = -Cr/2$ and $w^{(o)} = Cz$ [Eqs. (2.1)] at the two boundaries of the computational domain indicated in Fig. 1, where $C = Ga\mu_o/\sigma$ is the capillary number. The outflow boundary conditions $F_z = u_z^{(i)} = w_z^{(i)} = 0$ are prescribed in the jet outlet cross-section, while the symmetry plane condition is considered on the left-hand side of the outer computational domain.

For $Q > 0$, the parabolic velocity profile corresponding to the dimensionless flow rate $Q = Q_i/(\pi a^2 \sigma/\mu_o)$ is imposed inside the feeding capillary at a distance L_0 from its exit ($L_0 = 5$ in the simulations unless otherwise stated). The flow with $Q = 0$ is simulated by extending the symmetry plane condition to the capillary exit (Fig. 2). This case corresponds to a droplet submerged in an extensional flow with its equator pinned to an
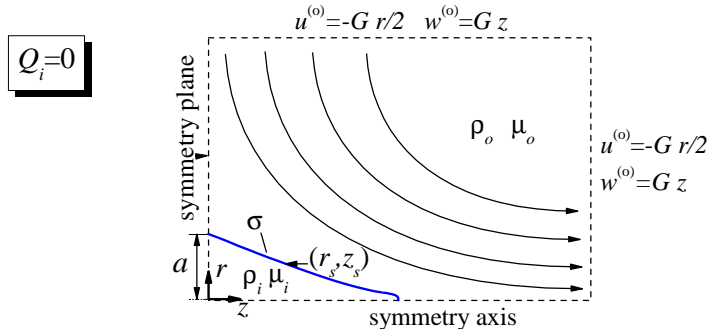
FIGURE 2. Sketch of the fluid domain for $Q = 0$. The dashed line indicates the computational domain.

infinitely thin ring. If $Q = 0$, the droplet volume

$$V = \frac{\pi}{2} \int_0^\Lambda F^2 \, dz \qquad (2.7)$$

is prescribed, where Λ is the droplet length $(F(\Lambda) = 0)$.

For a fixed value of L_0, the problem with $Q > 0$ is formulated in terms of the dimensionless numbers $\{\lambda, C, \mathrm{Re}_i, \mathrm{Re}_o, Q\}$, which reduce to $\{\lambda, C, Q\}$ when inertia is neglected. We will consider this approximation in most of our analysis. The viscosity ratio and Reynolds numbers are defined in terms of material properties and the capillary radius, which allows fixing their values in an experimental run in which the strain rate (the capillary number) and injected flow rate are changed. These two variables are the experimental operational parameters. For $Q = 0$, the problem is formulated in terms of the dimensionless numbers $\{C, \mathrm{Re}_i, \mathrm{Re}_o, V\}$.

To calculate the linear global modes of the steady solution, we assume the temporal dependence

$$U = U_0 + \delta U \, e^{-i\omega t} \quad (|\delta U| \ll |U|), \qquad (2.8)$$

where U represents any unknowns of the problem, and U_0 and δU stand for the corresponding base flow (steady) solution and the spatial dependence of the eigenmode, respectively. For $Q > 0$, we assume the temporal dependence for the interface location

$$F = F_0 + \delta F \, e^{-i\omega t} \quad (|\delta F| \ll F_0), \qquad (2.9)$$

where F_0 denotes the interface position in the base flow, and δF is the perturbation. For $Q = 0$, the interface location is defined in terms of intrinsic coordinates. In this case, we assume the temporal dependence

$$(r_s, z_s) = (r_{s0}, z_{s0}) + (\delta r_s, \delta z_s) \, e^{-i\omega t} \quad (|\delta r_s| \ll r_{s0}, |\delta z_s| \ll z_{s0}), \qquad (2.10)$$

where (r_{s0}, z_{s0}) is the droplet shape in the base flow, and $(\delta r_s, \delta z_s)$ is the perturbation. In the above equations, $\omega = \omega_r + i\omega_i$ is the eigenfrequency characterizing the perturbation evolution. If the growth rate ω_i^* of the dominant mode (i.e., that with the largest ω_i) is positive, then the base flow is asymptotically unstable under small-amplitude perturbations (Theofilis 2011).

We used a boundary-fitted spectral method (Herrada & Montanero 2016) to solve the theoretical model described above. Here, we summarize the main characteristics of this method. The inner and outer fluid domains are mapped onto two quadrangular domains through non-singular mapping. A quasi-elliptic transformation (Dimakopoulos & Tsamopoulos 2003) is applied in the outer bath. All the derivatives appearing
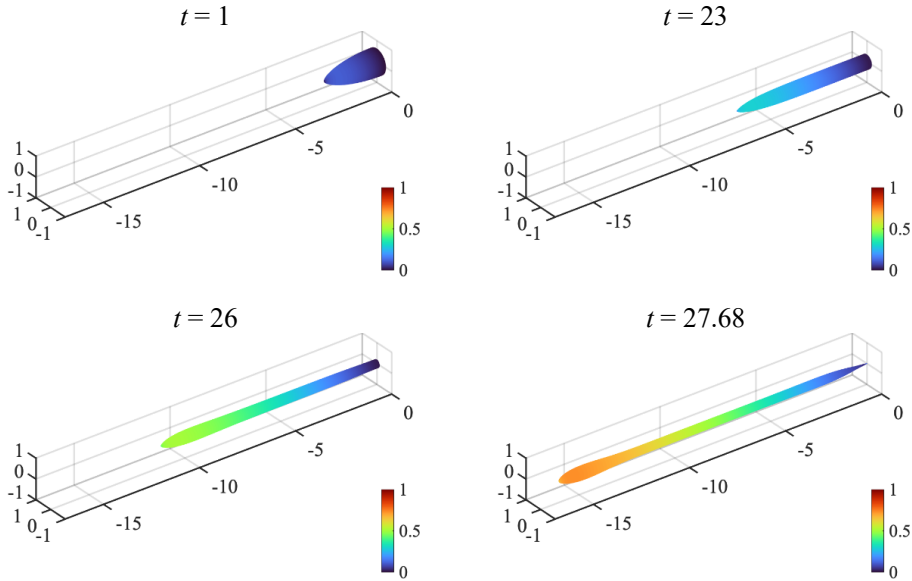
FIGURE 3. Half droplet shape at the end of a transient simulation for $\text{Re}_i = \text{Re}_o = 0$, $\lambda = 0.0125$, and $C = 0.26$. The color scale indicates the magnitude of the interface velocity relative to the magnitude of the imposed external flow at that point.

in the governing equations are expressed in terms of the spatial coordinates resulting from the mapping. These equations are discretized in the (mapped) radial direction with Chebyshev spectral collocation points (Khorrami *et al.* 1989). We use fourth-order finite differences with equally spaced points to discretize the (mapped) axial direction.

We conduct transient numerical simulations for $Q = 0$. Second-order backward finite differences are used to discretize the time domain. The time step is adapted in the course of the simulation according to the formula $\Delta t = \Delta t_0 / v_{\text{tip}}$, where Δt_0 is the time step at the initial instant, and v_{tip} is the droplet tip velocity. The time-dependent mapping of the physical domain does not allow the algorithm to go beyond the interface pinch-off. Therefore, the evolution of the emitted droplet cannot be analyzed using the present code.

3. Results

3.1. *The case $Q = 0$*

Consider a droplet suspended in an extensional uniaxial flow, as shown schematically in Fig. 2. The viscous force exerted by the outer fluid deforms the droplet, which adopts an oblate shape. The magnitude of this deformation increases with the capillary number. The droplet apex sharpens in the direction of the outer flow as λ decreases. The viscosity force drives a steady recirculation flow inside the droplet. For sufficiently large values of the capillary number, this flow becomes unstable at a saddle-node bifurcation, which corresponds to a turning point when the droplet deformation $D = (\hat{a} - \hat{b})/(\hat{a} + \hat{b})$ ($\hat{a}$ and $\hat{b}$ are the half-length and half-breadth of the cross-sectional shape, respectively) is plotted against the capillary number (Taylor 1964; Acrivos & Lo 1978). Both the real and imaginary parts of the critical eigenfrequency vanish at the bifurcation. The critical non-oscillatory eigenmode leads to the so-called central pinching mode, producing the thinning of the droplet equator until the interface pinches (Herrada *et al.* 2022) (Fig. 3).
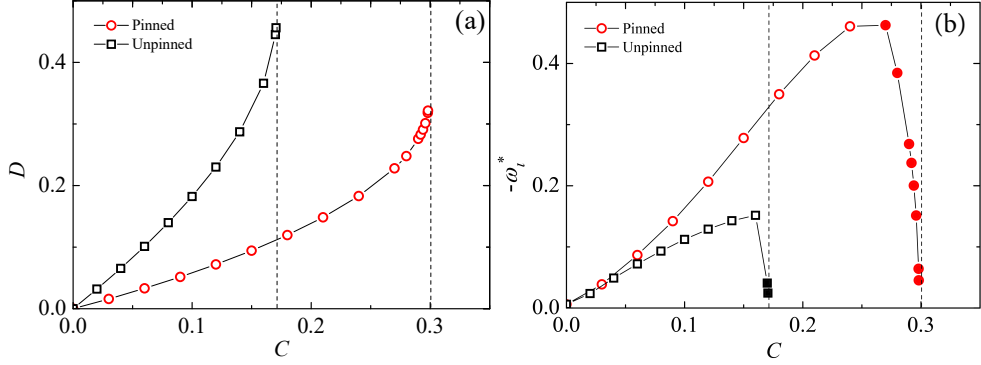
FIGURE 4. (a) Droplet deformation D and (b) growth rate of the dominant mode, ω_i^*, versus the capillary number C. The results were calculated as a function of the capillary number C for $\mathrm{Re}_i = \mathrm{Re}_o = 0$ and $\lambda = 0.1$. The circles (squares) correspond to the pinned (unpinned) droplet. The dotted lines indicate the critical capillary numbers. The solid symbols show the crossover of two modes.
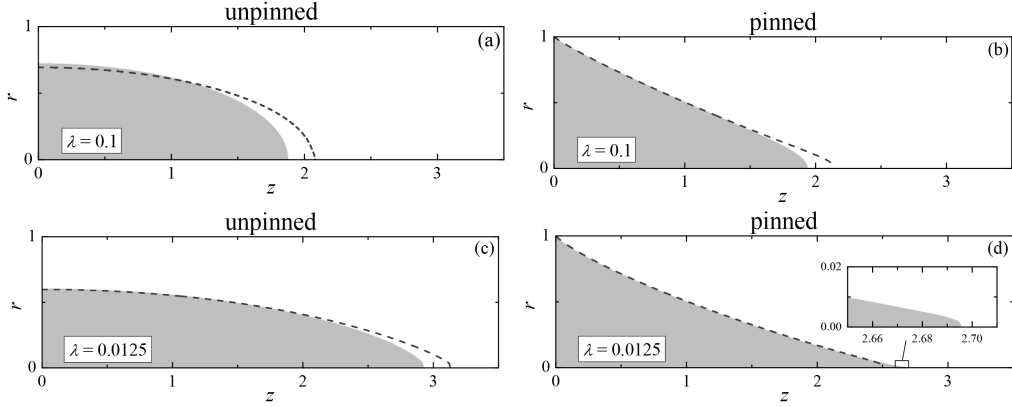

FIGURE 5. Droplet shape in the base flow, (r_{s0}, z_{s0}) (shaded area), and interface displacement due to the critical linear eigenmode, $(r_s, z_s) = (r_{s0}, z_{s0}) + \phi\left(\mathrm{Re}[\delta r_s], \mathrm{Re}[\delta z_s]\right)$ (dashed lines), for $\lambda = 0.1$ and $C = 0.17$ (a), $\lambda = 0.1$ and $C = 0.30$ (b), $\lambda = 0.0125$ and $C = 0.25$ (c), and $\lambda = 0.0125$ and $C = 0.55$ (d). The value of the arbitrary constant ϕ in the linear analysis has been chosen to appreciate the interface deformation.

The simulations conducted in this work for $Q = 0$ correspond to the problem described above except for a fundamental difference: the droplet equator is a triple contact line pinned to the feeding capillary edge in the present study. This last condition suppresses the central pinching mode described above, considerably increasing the critical capillary number (Fig. 4). As in the unpinned droplet case, the pinned droplet reaches a saddle-node bifurcation. However, the critical perturbation is localized in the droplet tip (Fig. 5), giving rise to microdripping (Fig. 6) instead of the central pinching mode.

The critical capillary number increases as λ decreases. Consequently, the droplet stretches at the stability limit, the outer velocity around the droplet tip considerably increases, and the tip curvature grows. For small values of λ, the microdripping mode produces tiny droplets much smaller than the mother drop (Fig. 6). The effect of the contact line pinning is somewhat similar to covering the droplet with a surfactant monolayer (Eggleton *et al.* 2001; Herrada *et al.* 2022).
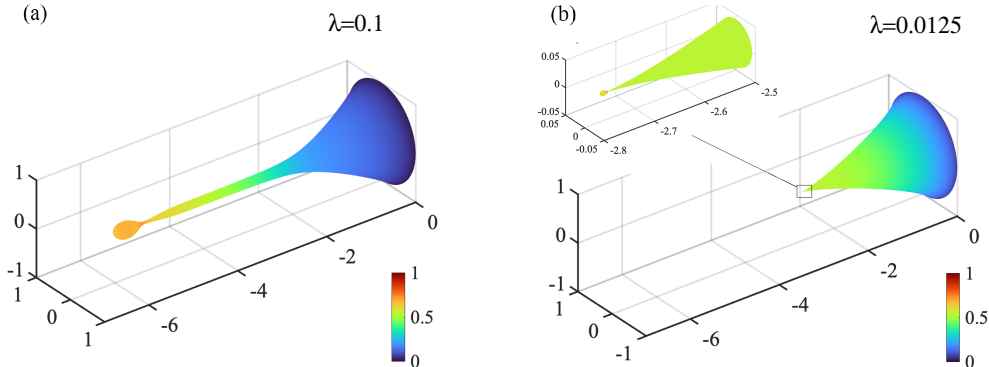
FIGURE 6. Droplet shape at the end of a transient simulation for $\text{Re}_i = \text{Re}_o = 0$. The images correspond to $\lambda = 0.1$ (a) and $\lambda = 0.0125$ (b), and their respective critical capillary numbers are $C = 0.31$ and 0.56. The color scale indicates the magnitude of the interface velocity relative to the magnitude of the imposed external flow at that point. The triple contact line is pinned to the feeding capillary edge.
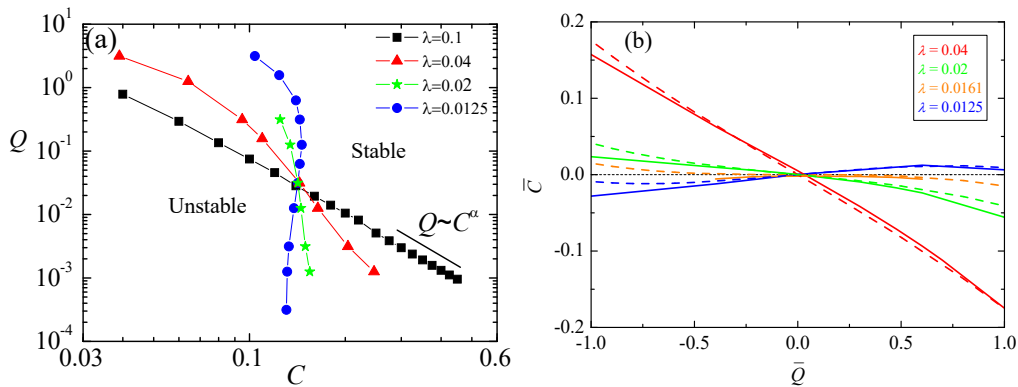

FIGURE 7. (a) Stability map for viscosity-dominated flow ($\text{Re}_i = \text{Re}_o = 0$). The symbols correspond to marginally stable ($\omega_i^* = 0$) microjetting realizations. (b) Fitting (3.1) to the simulation results. The solid lines are splines through the simulation data, and the dashed lines correspond to Eq. (3.1) with $Q^* = 0.0314$, $C^* = 0.142$, $a_1 = 6.71$, $\lambda^* = 0.0161$, and $c_3 = 0.015$.

3.2. *The case $Q > 0$*

We now focus on the more interesting case $Q > 0$, where a fluid is injected at a constant rate through the feeding capillary placed in the extensional flow. We first consider flows dominated by viscosity ($\text{Re}_i = \text{Re}_o = 0$), characterized only by the viscosity ratio λ, the capillary number C, and the injected flow rate Q. The effect of inertia will be analyzed at the end of this section.

Figure 7a shows the stability map in the parameter plane (C,Q) for several values of the viscosity ratio λ. We could not conduct simulations for $Q \lesssim 10^{-4}$ because of the sharp increase in the computing time caused by the much smaller flow scales generated as Q decreases. The symbols correspond to marginally stable cases for which $\omega_i^* = 0$.

In all the cases, $\omega_r^* \neq 0$, which means that the flow becomes unstable due to an oscillatory supercritical Hopf bifurcation linked to the presence of the jet. The jet convects capillary modes, which translates into an oscillatory behavior in the Eulerian frame of reference. In fact, this oscillatory instability has been observed in the microjetting mode

of all the configurations analyzed so far (Montanero & Gañán-Calvo 2020). The growth of the interface oscillation eventually produces the interface pinching, and the system evolves from steady microjetting towards some type of dripping.

The results reveal an interesting dependence of the critical capillary number on λ for a fixed flow rate. All the stability curves approximately intersect at $Q = Q^* \simeq 0.031$ and $C = C^* \simeq 0.15$. For $Q \gtrsim 0.031$, the critical capillary number decreases as λ increases, while the opposite occurs for $Q \lesssim 0.031$. We conclude that the inner viscosity stabilizes the flow for $Q \gtrsim 0.031$ but destabilizes it for sufficiently small flow rates.

Increasing the capillary number stabilizes the jet. In other words, there is a critical curve $C(Q, \lambda)$ at which the growth rate vanishes and the flow passes from unstable to stable. As mentioned above, there is a critical flow rate $Q^* \simeq 0.031$ for which the critical number $C^* \simeq 0.15$ is practically independent of λ. This suggests introducing the parameters $\bar{Q} = \log_{10} Q - \log_{10} Q^*$ and $\bar{C} = \log_{10} C - \log_{10} C^*$. For a critical viscosity ratio $\lambda = \lambda^*$, one expects $\partial \bar{C} / \partial \bar{Q} = 0$ at $\bar{C} = \bar{Q} = 0$. In addition, the curve $\bar{C}(\bar{Q})$ should be invertible as $\lambda - \lambda^*$ passes from negative to positive values. This suggests a bifurcation of the form

$$\bar{C} = a_1 (\lambda - \lambda^*) \bar{Q} - c_3 \bar{Q}^3. \tag{3.1}$$

Fitting this expression to the numerical simulations leads to $Q^* = 0.0314$, $C^* = 0.142$, $a_1 = 6.71$, $\lambda^* = 0.0161$, and $c_3 = 0.015$ (Fig. 7b).

Two types of asymptotic behavior of the stability limit $Q(C)$ can be observed in Fig. 7a as $Q \to 0$. For $\lambda \geqslant 0.02$, $Q \sim C^\alpha$ with $\alpha < 0$, which implies that, for any value of C, there is a finite value of Q below which the steady flow becomes unstable. This is the expected behavior because it corresponds to what has been observed in all tip streaming configurations (Montanero & Gañán-Calvo 2020). In contrast, $Q(C)$ seems to approach a vertical asymptote $C = 0.131$ for $\lambda = 0.0125$. This means that the flow remains stable for infinitely small values of Q provided that $C \geqslant 0.131$. This result constitutes the central finding of this work.

The above conclusion has obvious practical consequences. The jet diameter scales as $Q^{1/2}$ at a fixed distance from the feeding capillary, and hence fluid jets with vanishing diameters can be steadily emitted as $Q \to 0$. As the outer viscosity increases at a fixed jet viscosity and outer flow intensity, λ decreases, and C increases. For $\lambda < \lambda^*$ and C sufficiently large, one is in the stable regime of Fig. 7a, and arbitrarily thin jets can be realized. We conclude that jets with vanishing diameters can be produced for a large enough outer viscosity, independently of the jet viscosity and outer flow intensity. For a fixed outer viscosity, infinitely thin jets can also be produced if the jet viscosity (the viscosity ratio λ) is sufficiently small and the flow intensity (the capillary number C) is large enough.

We now analyze the case $\lambda = 0.0125$ in more detail in Fig. 8. This figure compares the critical capillary number $C_c(Q)$ for microjetting with the value C_{c0} obtained for a pinned droplet ($Q = 0$) (see Sec. 3.1) with the same volume as that of the microjetting meniscus (red circles in Fig. 8). The meniscus volume is calculated as that delimited by the end of the feeding capillary and the stagnation point in front of the jet. This volume hardly changes for $\lambda = 0.0125$ and $Q < 0.05$. For this reason, C_{c0} is practically constant in all the cases considered. As explained above, microjetting becomes unstable for $C < C_c$, while the droplet becomes unstable for $C > C_{c0}$.

In all the cases considered in Fig. 8, $C_{c0} < C_c(Q)$. This can be interpreted as follows. Consider a pinned drop of a given volume submerged in an extensional flow characterized by the capillary number C. The drop stretches and approaches its stability limit as C increases. At the critical capillary number $C = C_{c0}$, the drop tip destabilizes (Fig. 5)
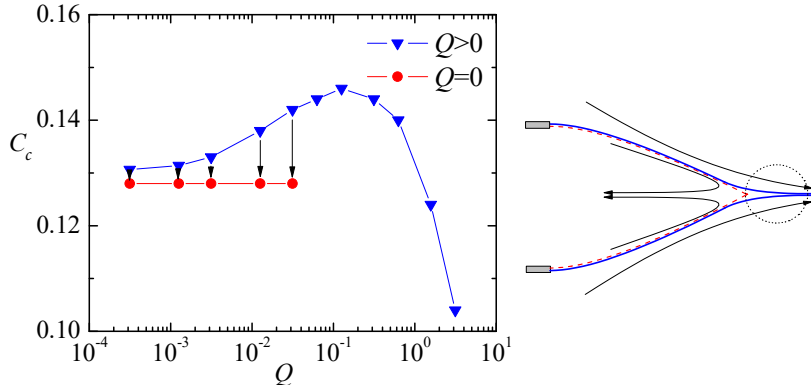
FIGURE 8. (Left) Critical capillary number C_c as a function of the flow rate Q for viscosity–dominated flow ($Re_i = Re_o = 0$) and $\lambda = 0.0125$ (blue triangles). The red circles indicate the critical capillary C_{c0} for the onset of instability for a droplet with the same volume as that of the meniscus of the corresponding microjetting realization, as indicated by the arrows. (Right) Sketch of the microjetting mode and its closed-droplet counterpart.

and ejects a tiny droplet (Fig. 6). However, the capillary number is not large enough to maintain the liquid ejection, and the steady microjetting mode is not established. If the flow rate Q is appropriately selected, and the capillary number is further increased up to $C = C_c(Q)$, a marginally stable microjetting realization is produced with a meniscus volume equal to that of the pinned drop. Therefore, each marginally stable pinned drop has its marginally stable "microjetting counterpart".

Neither the drop nor its microjetting counterpart is stable in the interval $C_{c0} < C < C_c(Q)$. This interval is expected to correspond to some type of dripping. The interval $C_{c0} < C < C_c(Q)$ decreases as Q decreases because the size of the critical cone-jet transition region (the region marked with a circle in Fig. 8-right) decreases as Q decreases. We calculated the oscillation frequency ω_r^* of the critical eigenmode for $Q > 0$ and verified that $\omega_r^* \to 0$ for $Q \to 0$. However, this oscillatory Hopf bifurcation becomes a non-oscillatory saddle-node bifurcation ($\omega_r^* = 0$) only at $Q = 0$ due to the system "discontinuous" topological change from jetting to a closed-droplet at $Q = 0$.

As explained above, the viscosity ratio λ essentially determines the fate of the microjetting mode as the flow rate decreases. In the limit $Q \to 0$, the microjetting mode remains stable for sufficiently small values of λ and destabilizes otherwise. Figure 9 shows how the tapering meniscus shape changes when the flow rate is reduced by a factor of 100. For $\lambda = 0.1$, the entire meniscus shrinks. Conversely, most part of the cone keeps the same shape for $\lambda = 0.0125$. Only the cone-jet transition region collapses.

As explained above, for a fixed and sufficiently small flow rate, the critical capillary number decreases as λ decreases (Fig. 7). Figure 10 shows the streamlines of the marginally stable base flow for $\lambda = 0.1$ and 0.0125 and the same flow rate $Q = 0.00126$. For $\lambda = 0.1$, the inner viscosity enhances the diffusion of axial momentum from the interface toward the tapering meniscus, the inner fluid accelerates, the meniscus shrinks and adopts a funnel-like shape, and the recirculation cells enter the feeding tube. For $\lambda = 0.0125$, the tapering meniscus stretches and adopts a slender quasi-conical shape predicted by the slender body theory. In this case, the recirculation cell hardly enters the feeding tube.

Figure 11 shows the increase of the recirculation cell size as the injected flow rate decreases. The recirculation cell size S_r is determined as the distance between the front and rear stagnation points on the symmetry axis. In the two cases analyzed, S_r becomes
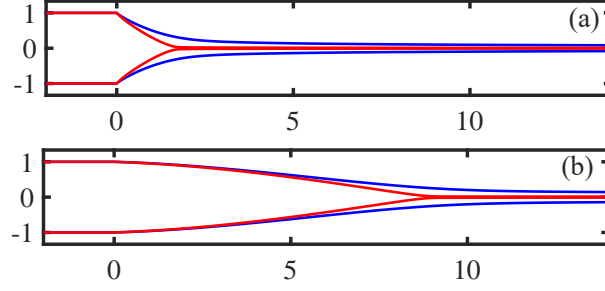
FIGURE 9. (a) Meniscus shape for $\lambda = 0.1$, $C = 0.425$, and $Q = 0.126$ (blue lines) and $Q = 0.00126$ (marginally stable flow) (red lines). (b) Meniscus shape for $\lambda = 0.0125$, $C = 0.132$, and $Q = 0.126$ (blue lines) and $Q = 0.00126$ (marginally stable flow) (red lines). In all the simulations, $\mathrm{Re}_i = \mathrm{Re}_o = 0$.
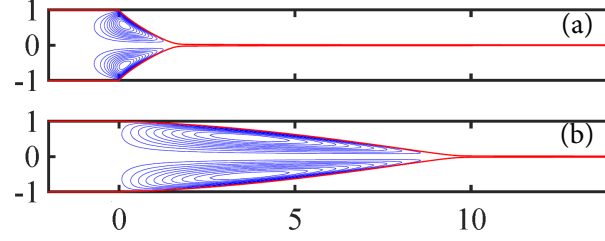

FIGURE 10. Streamlines of the marginally stable base flow for ($\lambda = 0.1$, $C = 0.425$, $Q = 0.00126$) (a) and ($\lambda = 0.0125$, $C = 0.130$, $Q = 0.00126$) (b). In the two cases, $\mathrm{Re}_i = \mathrm{Re}_o = 0$. For sufficiently small λ, the recirculating cells do not enter the feeding tube.
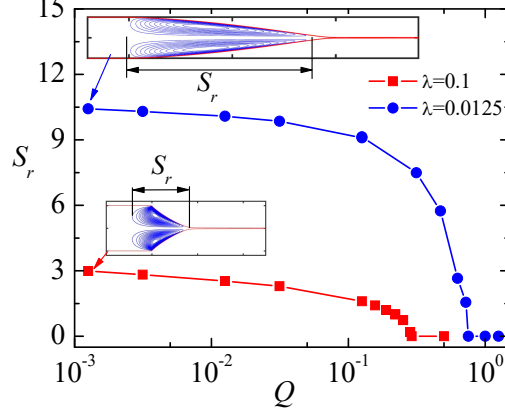

FIGURE 11. Size of the recirculation cell, S_r, as a function of the flow rate Q for ($\lambda = 0.1$, $C = 0.425$) (squares) and ($\lambda = 0.0125$, $C = 0.130$) (circles). In the two cases, $\mathrm{Re}_i = \mathrm{Re}_o = 0$. The insets show the streamlines for the marginally stable cases (Fig. 7).

approximately constant as Q decreases for values of the injected flow rate much larger than the critical one. This behavior differs substantially from that observed in other tip streaming configurations, such as gaseous flow focusing, where S_r is a linear function of Q below a threshold value of the flow rate (Herrada *et al.* 2008). For $\lambda = 0.0125$ and $C = 0.130$, the recirculation cell remains practically at the same position as Q decreases, while it slightly displaces backward for $\lambda = 0.1$ and $C = 0.425$. As shown below, the penetration of the recirculating cell into the tube may be a destabilizing factor.

It has been hypothesized that the microjetting mode of configurations such as gaseous
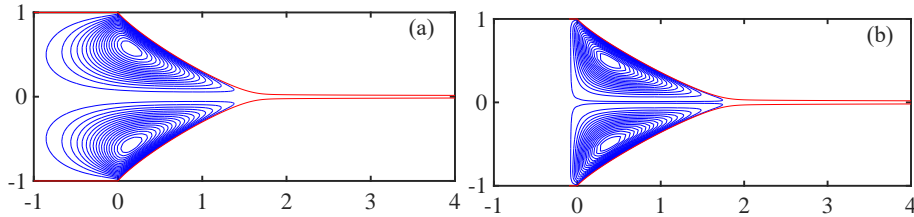
FIGURE 12. Streamlines of the marginally stable base flow for ($\lambda = 0.1$, $Q = 0.00126$, $\mathrm{Re}_i = 0$, $\mathrm{Re}_o = 0$). The graph (a) corresponds to $L_0 = 5$ and $C = 0.42$, and the graph (b) corresponds to $L_0 = 0$ and $C = 0.38$.

flow focusing (Gañán-Calvo 1998) becomes unstable at the minimum flow rate stability limit because the recirculation cells enter the feeding tube, limiting the flow rate that can recirculate in the tapering meniscus and, therefore, setting a minimum value for the injected flow rate (Herrada *et al.* 2008). To investigate this possibility, we conducted numerical simulations for $L_0 = 0$, i.e., imposing the inlet boundary condition at the tube exit to expel the recirculation cells. Figure 12 shows the streamlines of the marginally stable flows for $\lambda = 0.1$ and $L_0 = 0$ and 5 defined in Fig. 1.

For $\lambda = 0.0125$, the stability limit was practically the same, which indicates that the penetration of the recirculation had a negligible effect on the microjetting stability. This is consistent with the idea that the conditions at the cone-jet transition region essentially determine the flow stability for $\lambda = 0.0125$. The same approximation has been considered to predict the minimum flow rate stability limit of electrospray (Gañán-Calvo *et al.* 2013). For $\lambda = 0.1$, expelling the recirculation cells from the tube displaces the front stagnation point downstream and stabilizes the microjetting mode so that the critical capillary number decreases from $C = 0.42$ to 0.38. It is worth mentioning that the meniscus funnel-like shape for $\lambda = 0.1$ resembles that of gaseous flow focusing (Montanero & Gañán-Calvo 2020).

The results discussed above indicate that the coupling between the recirculation and the flow in the feeding capillary is a destabilizing factor. This coupling can be quantified through the wall shear stress averaged over the capillary inner surface. We define τ_w as that stress normalized with the value corresponding to the (unperturbed) Poiseuille flow. The destabilizing interaction between the recirculation and the flow in the feeding capillary is much more intense for $\lambda = 0.1$ (Fig. 13). In this case, the penetration of the recirculation cells into the tube produces an increase in two orders of magnitude of the friction with the wall. This increase is localized near the feeding capillary edge, where the shear rate peaks. This effect is much less noticeable for $\lambda = 0.0125$.

The convective motion at the cone-jet transition region for small values of λ is expected to stabilize the flow. This mechanism can be quantified by the ratio C_{tip}/C, where $C_{\mathrm{tip}} = v_{\mathrm{tip}}^{(o)} \mu_o / \sigma$ is the capillary number at the tip, and $v_{\mathrm{tip}}^{(o)}$ is the uniaxial extensional flow velocity at the front stagnation point. The ratio C_{tip}/C measures the increased strength of the outer flow in the tip due to the meniscus stretching. Figure 14 shows the dependence of C_{tip}/C and τ_w on the injected flow rate Q for fixed values of the capillary number. For $\lambda = 0.0125$, the cone sharply stretches as the flow rate decreases and reaches an approximately constant size for $Q \lesssim 10^{-1}$. This stabilizing effect is much less noticeable in the case $\lambda = 0.1$.

The above results suggest that the flow in the cone-jet transition for $\lambda = 0.0125$ is practically decoupled from that in the rest of the cone, while the flow in the tip of the funnel-like meniscus for $\lambda = 0.1$ is affected by the inner fluid motion upstream. This is consistent with the spatial dependence of the perturbation of the interface contour, δF,
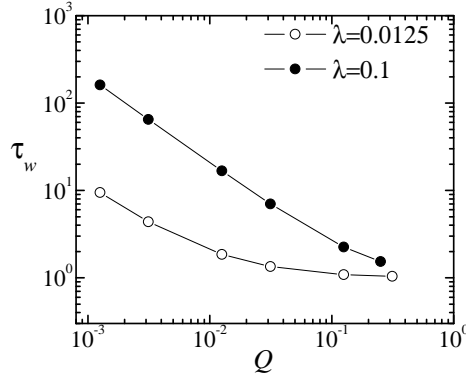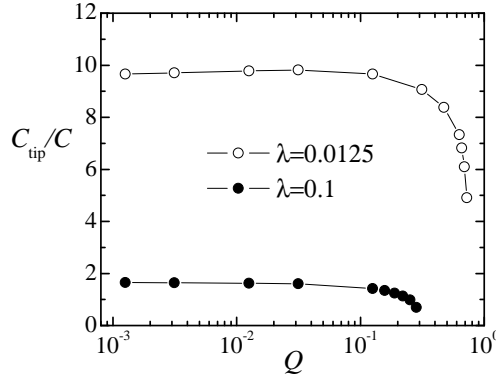
FIGURE 13. τ_w as a function of the flow rate Q for ($\lambda = 0.0125$, $C = 0.130$) (open symbols) and ($\lambda = 0.1$, $C = 0.425$) (solid symbols). In the two cases, $\mathrm{Re}_i = \mathrm{Re}_o = 0$.

FIGURE 14. C_{tip}/C as a function of the flow rate Q for ($\lambda = 0.0125$, $C = 0.130$) (open symbols) and ($\lambda = 0.1$, $C = 0.425$) (solid symbols). In the two cases, $\mathrm{Re}_i = \mathrm{Re}_o = 0$.
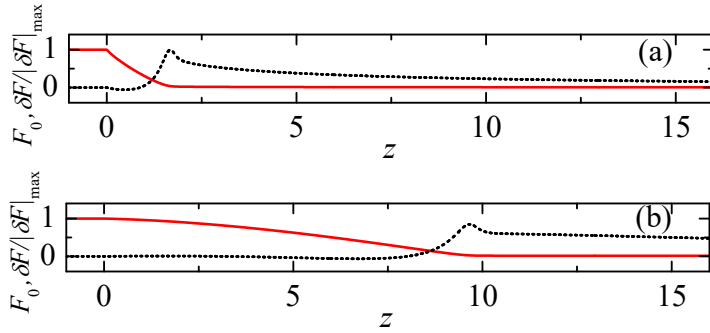

FIGURE 15. Interface contour (red solid line) and magnitude of the interface perturbation, $|\delta F|$ (black dotted line), for ($\lambda = 0.1$, $C = 0.425$, $Q = 0.00126$) (a) and ($\lambda = 0.0125$, $C = 0.130$, $Q = 0.00126$) (b). The magnitude of the interface perturbation has been normalized with its maximum value $|\delta F|_{\mathrm{max}}$. In the two cases, $\mathrm{Re}_i = \mathrm{Re}_o = 0$.

obtained in these two cases (Fig. 15). While $|\delta F| \simeq 0$ in the cone for $\lambda = 0.0125$, the meniscus contour is perturbed in front of its tip for $\lambda = 0.1$.

All the previous results were obtained for $\mathrm{Re}_i = \mathrm{Re}_o = 0$. Figure 16 shows the effect of the inner fluid inertia on the stability map. We did not study the influence of the outer fluid inertia because the numerical method did not converge to the solution for
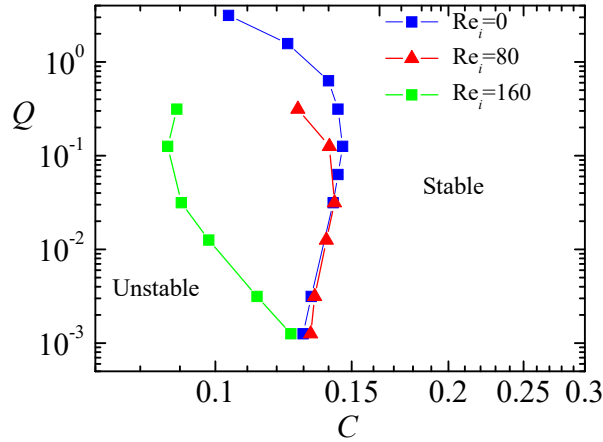
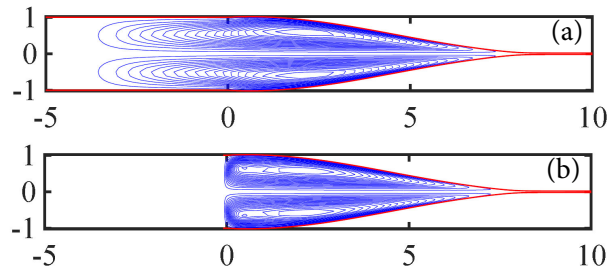FIGURE 16. Stability limit for $\lambda = 0.0125$ and $\mathrm{Re}_o = 0$.

FIGURE 17. Streamlines of the marginally stable base flow for ($\lambda = 0.0125$, $C = 0.13$, $Q = 0.00126$, $\mathrm{Re}_i = 160$, $\mathrm{Re}_o = 0$). Graphs (a) and (b) correspond to $L_0 = 5$ and 0, respectively (for $L = 0$, the parabolic velocity profile is imposed at $z = 0$). The critical capillary number is practically the same in the two cases.

large values of Re_o. The behavior for $Q \to 0$ is not significantly affected by inertia for $\mathrm{Re}_i = 80$. However, the extrapolation of the stability curve for $\mathrm{Re}_i = 160$ indicates that, for any capillary number, there is a minimum flow rate below which microjetting becomes unstable, as occurs for larger values of λ and in the rest of the tip streaming configurations (Montanero & Gañán-Calvo 2020). The inner fluid inertia makes the recirculation cells enter the feeding capillary (Fig. 17). When the cells are expelled from the capillary, the front stagnation point does not move, and the critical capillary number hardly changes, which confirms that instability is linked to the flow in the tiny cone-jet transition region.

4. Conclusions

The simulations for zero injected flow rate show that a droplet attached to a feeding capillary and submerged in a linear extensional flow produces microdripping. The size of the ejected droplet becomes extremely small for low values of the viscosity ratio. This occurs because the pinning of the triple contact line suppresses the central pinching mode, enabling the stretching of the droplet and the increase of the droplet tip curvature at the stability limit.

We have shown that the linear extensional flow can produce jets with arbitrarily small diameters, provided that the viscosity of the outer fluid is sufficiently high. In this case, a slender conical meniscus forms attached to the feeding capillary. The cone-jet transition region becomes vanishingly small as the flow rate (the jet diameter) decreases. The

disparity between the size of this region and that of the meniscus suggests that the microjetting stability is determined by the flow in the cone-jet transition region.

Two mechanisms have been proposed to explain the effect of the viscosity ratio on the flow stability: (i) the convective motion at the cone-jet transition region, which stabilizes the flow for small values of λ, and (ii) the coupling between the recirculation and the flow in the feeding capillary, which may destabilize the flow for sufficiently large values of λ. Other destabilizing mechanisms linked to the recirculation have been proposed to explain the instability of tip streaming in other configurations. Cabezas *et al.* (2021) hypothesized that instability of liquid-liquid flow focusing may be caused by the displacement towards the interface of the recirculation cell, which narrows the stream tube across which the injected liquid leaves the meniscus. This and similar effects may also contribute to the instability of the flow analyzed in the present work for sufficiently large values of λ.

The velocity of the imposed extensional flow along the symmetry axis increases with the distance from the feeding capillary. This peculiarity seems to play a critical role in the microjetting stability. For sufficiently small values of the viscosity ratio, the meniscus stretches as the flow rate decreases. Therefore, the meniscus tip is exposed to larger outer fluid velocities as the flow rate decreases. This seems to stabilize the flow in the cone-jet transition region. We hope the present theoretical study will be a useful guide for experimentalists in their search for new microjetting techniques.

Our study reveals the importance of conducting the stability analysis of the base flow. In fact, our numerical method finds the solution to the steady governing equations regardless of whether the flow is linearly stable or unstable, which typically occurs when a Hopf bifurcation causes the instability.

REFERENCES

Acrivos, A. & Lo, T. 8. 1978 Deformation and breakup of a single slender drop in an extensional flow. *J. Fluid Mech.* **86**, 641–672.

Anna, S. L. & Mayer, H. C. 2006 Microscale tipstreaming in a microfluidic flow focusing device. *Phys. Fluids* **18**, 121512.

Cabezas, M. G., Rubio, M., Rebollo-Muñoz, N., Herrada, M. A. & Montanero, J. M. 2021 Global stability analysis of axisymmetric liquid-liquid flow focusing. *J. Fluid Mech.* **909**, A10.

Cruz-Mazo, F., Herrada, M. A., Gañán-Calvo, A. M. & Montanero, J. M. 2017 Global stability of axisymmetric flow focusing. *J. Fluid Mech.* **832**, 329–344.

De Bruijn, R. A. 1993 Tipstreaming of drops in simple shear flows. *Chem. Eng. Sci.* **48**, 277–284.

Dimakopoulos, Y. & Tsamopoulos, J. 2003 A quasi-elliptic transformation for moving boundary problems with large anisotropic deformations. *J. Comput. Phys.* **192**, 494–522.

Duft, D., Achtzehn, T., Muller, R., Huber, B. A. & Leisner, T. 2003 Coulomb fission: Rayleigh jets from levitated microdroplets. *Nature* **421**, 128.

Eggers, J. 2021 Theory of bubble tips in strong viscous flows. *Phys. Rev. Fluids* **6**, 044005.

Eggleton, C. D., Tsai, T.-M. & Stebe, K. J. 2001 Tip streaming from a drop in the presence of surfactants. *Phys. Rev. Lett.* **87**, 048302.

Evangelio, A., Campo-Cortés, F. & Gordillo, J. M. 2016 Simple and double microemulsions via the capillary breakup of highly stretched liquid jets. *J. Fluid Mech.* **804**, 550–577.

Gañán-Calvo, A. M. 1998 Generation of steady liquid microthreads and micron-sized monodisperse sprays in gas streams. *Phys. Rev. Lett.* **80**, 285–288.

Gañán-Calvo, A. M. 2008 Unconditional jetting. *Phys. Rev. E* **78**, 026304.

Gañán-Calvo, A. M., González-Prieto, R., Riesco-Chueca, P., Herrada, M. A. & Flores-Mosquera, M. 2007 Focusing capillary jets close to the continuum limit. *Nat. Phys.* **3**, 737–742.

Gañán-Calvo, A. M., Rebollo-Muñoz, N. & Montanero, J. M. 2013 Physical symmetries and scaling laws for the minimum or natural rate of flow and droplet size ejected by Taylor cone-jets. *New J. Phys.* **15**, 033035.

Herrada, M. A., Gañán-Calvo, A. M., Ojeda-Monge, A., Bluth, B. & Riesco-Chueca, P. 2008 Liquid flow focused by a gas: Jetting, dripping, and recirculation. *Phys. Rev. E* **78**, 036323.

Herrada, M. A & Montanero, J. M. 2016 A numerical method to study the dynamics of capillary fluid systems. *J. Comput. Phys.* **306**, 137–147.

Herrada, M. A., Ponce-Torres, A., Rubio, M., Eggers, J. & Montanero, J. M. 2022 Stability and tip streaming of a surfactant-loaded drop in an extensional flow. influence of surface viscosity. *J. Fluid Mech.* **934**, A26.

Khorrami, M. R., Malik, M. R. & Ash, R. L. 1989 Application of spectral collocation techniques to the stability of swirling flows. *J. Comput. Phys.* **81**, 206–229.

López, M., Cabezas, M. G., Montanero, J. M. & Herrada, M. A. 2022 On the hydrodynamic focusing for producing microemulsions via tip streaming. *J. Fluid Mech.* **934**, A47.

Montanero, J. M. & Gañán-Calvo, A. M. 2020 Dripping, jetting and tip streaming. *Rep. Prog. Phys.* **83**, 097001.

Ponce-Torres, A., Rebollo-Muñoz, N., Herrada, M. A., Gañán-Calvo, A. M. & Montanero, J. M. 2018 The steady cone-jet mode of electrospraying close to the minimum volume stability limit. *J. Fluid Mech.* **857**, 142–172.

Rubio-Rubio, M., Sevilla, A. & Gordillo, J. M. 2013 On the thinnest steady threads obtained by gravitational stretching of capillary jets. *J. Fluid Mech.* **729**, 471–483.

Suryo, R. & Basaran, O. A. 2006 Tip streaming from a liquid drop forming from a tube in a co-flowing outer fluid. *Phys. Fluids* **18**, 082102.

Taylor, G. 1964 Disintegration of water drops in electric field. *Proc. R. Soc. Lond. A* **280**, 383–397.

Taylor, G. I. 1932 The viscosity of a fluid containing small drops of another fluid. *Proc. R. Soc. Lond. A* **138**, 41–48.

Taylor, G. I. 1934 The formation of emulsions in definable fields of flow. *Proc. R. Soc. London, Ser. A* **146**, 501–523.

Theofilis, V. 2011 Global linear instability. *Annu. Rev. Fluid Mech.* **43**, 319–352.

Zhang, W. 2004 Viscous entrainment from a nozzle: Singular liquid spouts. *Phys. Rev. Lett.* **93**, 184502.